

Highly reduced iron-doped lithium niobate for optoelectronic tweezers

Michael Esseling · Annamaria Zaltron ·
Nicola Argiolas · Giovanni Nava · Jörg Imbrock ·
Ilaria Cristiani · Cinzia Sada · Cornelia Denz

Received: 14 December 2012 / Accepted: 15 April 2013 / Published online: 27 April 2013
© Springer-Verlag Berlin Heidelberg 2013

Abstract We investigate the applicability of highly reduced lithium niobate samples doped with iron for the use as optoelectronic tweezers. Increasing the reduction degree of Fe-doped lithium niobate is well known to increase the photoconductivity and reduce the writing time of internal space-charge fields. Based on our measurements of the photorefractive properties, we determine the optimal conditions for dielectrophoretic trapping and present the application of Fe-doped lithium niobate as optoelectronic tweezers. For higher reduction degrees, an unexpected decrease in the photovoltaic current density and the saturation space-charge field is reported.

1 Introduction

The field of optically induced micromanipulation, pioneered by Arthur Ashkin and coworkers with their seminal work on optical tweezers [1–3], has recently been enriched by the field of optoelectronic tweezers (OET), which are able to manipulate a myriad of particles with only a fraction of the power necessary for optical tweezers [4]. OET combine the strong forces originating from classical electrode-based dielectrophoresis (DEP) [5] with the optical

structuring of a photoconductive layer. The inhomogeneous illumination of this layer produces very flexible *virtual electrodes*; hence, OET benefit from their inherent optical reconfigurability as compared to their static counterparts that use micro-fabricated metal electrodes. In order to be able to generate high electric field gradients, which are necessary for efficient dielectrophoretic micromanipulation, without an external voltage supply, it has been proposed to employ lithium niobate (LiNbO₃) as the photoconductive layer in OET [6, 7]. LiNbO₃ provides the advantage that the high electric fields can be generated solely by the internal bulk photovoltaic effect [8]. In contrast to other DEP approaches, this redundantizes electrical connections and external voltage supplies, which implies that lithium niobate surfaces lend themselves to an easy integration into Lab-On-A-Chip devices. By doping the crystal with iron (Fe:LiNbO₃), the photorefractive response of the material is remarkably enhanced, obtaining values of the internal electric field in the range of several kV mm⁻¹, which are one order of magnitude larger than values measured in undoped crystals [9, 10]. Although multiplexing and switching of virtual electrodes in Fe:LiNbO₃ has been demonstrated [11], a significant drawback for the use of Fe:LiNbO₃ tweezers in real applications is still the relatively slow response of the internal fields for an as-grown sample. Therefore, it is necessary to speed up the photorefractive time constants of the material, that is to increase its photoconductivity. It is well known that an acceleration of recording can be accomplished by increasing the light intensity incident on the crystal. However, the available laser power poses an ultimate limit to this strategy. Another route to faster Fe:LiNbO₃ is to alter the reduction degree of the material [12, 13], which is the ratio between the concentration of filled (Fe²⁺) and empty (Fe³⁺) electron traps in the band transport model

M. Esseling (✉) · J. Imbrock · C. Denz
Institute of Applied Physics, University of Münster,
Corrensstrasse 2/4, 48149 Münster, Germany
e-mail: michael.esseling@uni-muenster.de

A. Zaltron · N. Argiolas · C. Sada
Physics and Astronomy Department, University of Padova,
via Marzolo 8, 35131 Padova, Italy

G. Nava · I. Cristiani
Dipartimento di Ingegneria Industriale e dell'Informazione,
University of Pavia, via Ferrata 1, 27100 Pavia, Italy

developed by Kukhtarev and coworkers [14]. In previous experiments, the photoconductivity was demonstrated to be linearly proportional to this reduction degree [12]. In this contribution, we focus our attention on the modification of the reduction degree of Fe:LiNbO₃ crystals to optimize the conditions for DEP manipulation on the surface.

2 Sample preparation

Several Fe:LiNbO₃ samples ($c_{\text{iron}} = 18.8 \times 10^{18} \text{ cm}^{-3}$, 0.1 % mol) with congruent composition were grown at the University of Padova by using the Czochralski technique. The growth direction was along the z axis of the material with a pulling rate of 2 mm h^{-1} . To obtain a single domain structure, the Fe:LiNbO₃ boule was poled in air atmosphere at $1,200^\circ$. Using X-ray diffraction, the crystalline quality of the grown samples was checked being compatible with commercial crystals. Consequently, the samples were oriented along the three main axes and cut in samples with the main face perpendicular to the y axis (y -cut). The samples were polished using a Logitech PM5 lapping machine to achieve optical quality surfaces. After the growth process and without any treatment, the iron in the lithium niobate crystal is mainly in its 3+ valence state, yielding an as-grown reduction degree of approx. 3 %. To increase the fraction of Fe²⁺, each sample underwent a reduction thermal treatment of varying time at 500°C in a gas mixture of Ar(98 %) + H₂(2 %), thus promoting the partial reduction of Fe³⁺ to Fe²⁺. To estimate the Fe²⁺/Fe³⁺ ratio, optical absorption measurements were taken in transmission mode with a Jasco V-670 spectrophotometer in the range 330–2,000 nm [15]. Fe²⁺ has a wide absorption band in the visible range, centered at 481 nm, whose intensity is proportional only to the concentration of filled traps [16]. Therefore, by measuring the light absorption at 532 nm and by knowing the corresponding cross section, it is possible to calculate the concentration of Fe²⁺ in each sample, deriving also the corresponding reduction degree, as reported for each crystal in the samples list in Table 1. Besides these reduced y -cut samples, a commercial as-grown y -cut crystal (Altechna) was considered for comparison.

3 Off-axis digital holographic setup

To characterize the photorefractive properties of the sample, the light-induced refractive index modulation was measured in the off-axis digital holographic setup shown in Fig. 1, which allows for a direct two-dimensional quantification of phase retardations without any previous assumptions or approximations [17]. The phase retardation

Table 1 Samples list

#	Name	Thickness $d/\mu\text{m}$	Fe ²⁺ /Fe ³⁺
1	AT1 (as-grown)	500	0.03 ± 0.003
2	151.1	780	0.08 ± 0.01
3	151.2	800	0.12 ± 0.02
4	151.6.1	250	0.36 ± 0.02
5	151.7	600	0.74 ± 0.05
6	151.12.1	250	1.63 ± 0.06
7	151.5.1	250	2.92 ± 0.11
8	151.10.1	250	3.49 ± 0.11
9	151.3	800	15.30 ± 1.34

The total iron concentration is $c_{\text{iron}} = 18.8 \times 10^{18} \text{ cm}^{-3}$ for all crystals

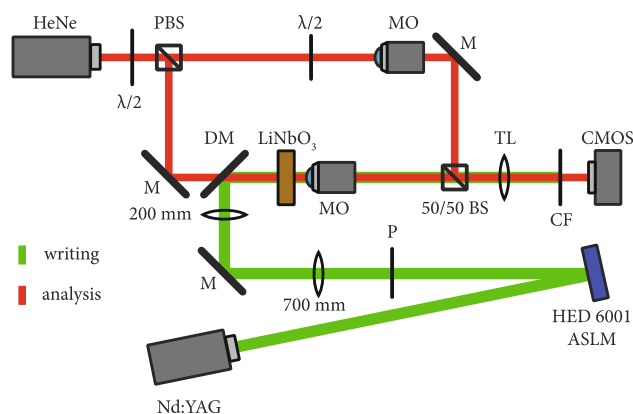
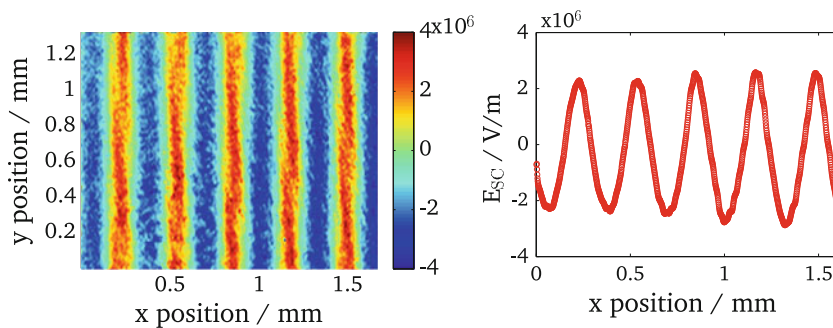


Fig. 1 Setup for the writing (green) and analysis (red) of internal photorefractive gratings in off-axis digital holography; ASLM amplitude spatial light modulator, CF color filter, (D)M (dichroic) mirror, MO microscope objective, (P)BS (polarizing) beam splitter, P polarisator, TL tube lens

upon propagation through the material was measured in a Mach-Zehnder-type interferometer and was used to calculate the internal electric field magnitude using the electro-optic effect [18, 19]. In order to induce a refractive index grating, an amplitude spatial light modulator (ASLM HES6001, Holoeye, Berlin) was illuminated using a frequency-doubled Nd:YAG laser and the resulting intensity pattern was demagnified onto the Fe:LiNbO₃ samples. A long-pass color filter just before the CCD suppressed the remaining green light. The writing beam was ordinarily polarized to minimize diffraction at the written refractive index grating. To determine the photorefractive parameters, the y -cut crystals were illuminated with a one-dimensional sinusoidal intensity pattern with its grating vector along the c axis. We acquired the two-dimensional phase modulation from our setup using a Hilbert transform and averaged along the constant direction (see also Fig. 2).

Fig. 2 Exemplary measurement of total electric field modulation: two-dimensional electric field modulation on crystal 151.7 after 48 s at $I = 62 \text{ mW cm}^{-2}$ (left) and field strength of the internal space-charge field averaged along the y direction (right)



Note that this special pattern and the one-dimensional averaging is only done to further improve the signal-to-noise-ratio. In principle, the same information about the electric field magnitude can be obtained for each single point and for binary patterns [11].

From the averaged data, we then determined the total modulation of the electric field $E_{SC} = E_{max} - E_{min}$ and the time response of the material by exploiting the simplified solutions of the Kukharev model [12]. To determine the temporal dynamics of the initial recording process with higher accuracy, a video of the initial grating formation was recorded for each of the samples at a frame rate of up to 20 fps. From these videos, the photovoltaic current density was obtained as a fit to the electric field evolution at the beginning of the recording process $j_{photo} = \epsilon\epsilon_0 \frac{\partial E}{\partial t} \Big|_{t \rightarrow 0}$. Together with the saturation field—obtained from a long-time measurement until the steady state was reached—we calculated the time constant of the sample as

$$\tau = \epsilon\epsilon_0 \frac{E_{max}}{j_{photo}}. \tag{1}$$

4 Results and discussion

4.1 Saturation space-charge field

The maximum space-charge field that can be created inside the material is a very important figure-of-merit for the use of lithium niobate for optoelectronic tweezers. The dielectrophoretic force for spherical particles in the case of low-frequency electric fields, which applies for Fe:LiNbO₃ as the substrate material [11], can be written as [20]

$$F_{DEP} = 2\pi r^3 \epsilon_m \frac{\sigma_p - \sigma_m}{\sigma_p + 2\sigma_m} \nabla E^2 \tag{2}$$

with the particle radius r , the static permittivity ϵ_m of the surrounding suspension medium (e.g., air or tetradecane), $\sigma_{p/m}$ as the DC conductivities of particle and medium, respectively, and the gradient of the electric field amplitude ∇E^2 . Hence, the force increases with the square of the electric field magnitude, allowing the exertion of substantially higher forces. From the theoretical description of the

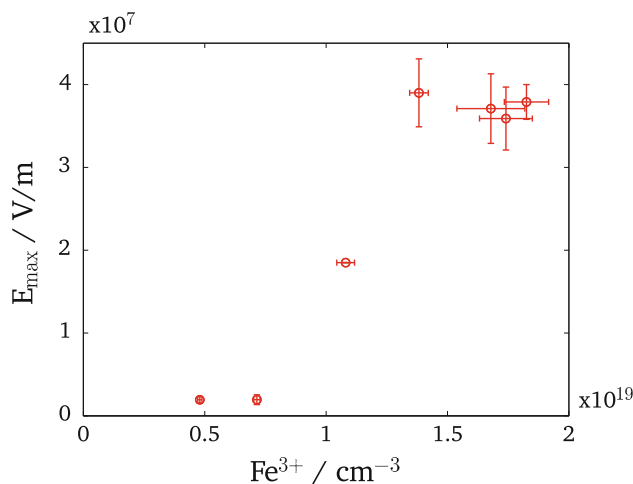


Fig. 3 Saturation field against Fe³⁺ concentration

charge transport processes, it follows that the electric field originates from electrons trapped in Fe³⁺ centers [12]. A linear decrease in the saturation field with the Fe³⁺ concentration is thus expected. In our experiments, we found that the saturation field for Fe³⁺ concentrations higher than $1.38 \times 10^{19} \text{ cm}^{-3}$ was constant within the measurement range (cf. Fig. 3). Of course, since the uncertainties from our measurement are rather large, a linear decrease with the Fe³⁺ lies within our results. What is unexpected is that for the more reduced samples, the saturation field was significantly lower, especially for samples 6 and 7 with a saturation field reduced by one order of magnitude ($1.94 \pm 0.01 \text{ kV mm}$ for sample 7). This behavior is not at all compliant with the theoretical description in [9] and points at the presence of different mechanisms of charge transport which decrease the saturation values of the space-charge field in the highly reduced samples. Further details about these processes can be found in the following sections.

4.2 Photovoltaic current density

The speed of the grating formation is in a first approximation determined by the photovoltaic current density that

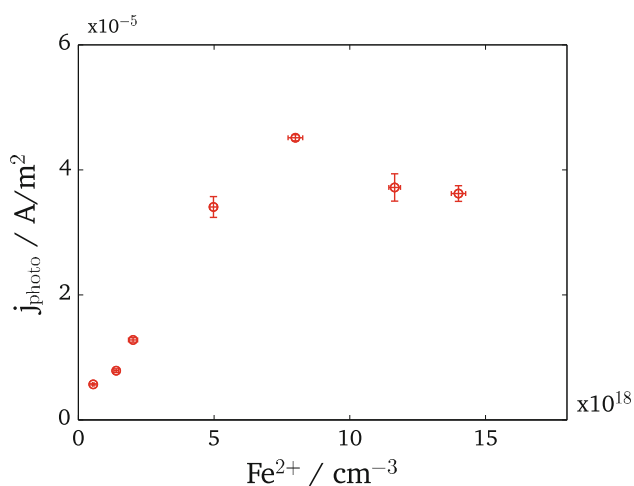


Fig. 4 Photovoltaic current density against Fe^{2+} concentration

is induced by the illumination. Figure 4 shows the results for the measurement of the photovoltaic current density versus the Fe^{2+} concentration. Due to the different thicknesses and absorption coefficients of the different crystals and the fact that our measurement is always an average over the whole thickness of the crystal, special care was taken to adjust the incident laser power so that the mean intensity along the length of the crystal was $I = 49 \pm 1$ mW cm^{-2} for each sample. From the theoretical model, a linear dependence of the current on the reduced iron center concentration would be expected [12]. However, in our measurements, such a linear dependence could only be found up to concentrations of $(8.00 \pm 0.54) \times 10^{18} cm^{-3}$, corresponding to a reduction degree of 0.74 ± 0.05 . On the contrary, for higher Fe^{2+} content (as in samples 6 and 7 with reduction degrees of more than 1.6), the value of the photovoltaic current density obtained by the fit decreases.

It is noteworthy that no refractive index grating could be recorded in samples with a reduction degree higher than 3, that is samples 8 and 9. Although these samples have undergone quite a long reduction treatment, from the measurement of the Fe^{2+} concentration, it can be concluded that a sufficient number of electron traps should still be present. Numerous contributions have focused their attention on the investigation of crystals with a variety of dopant concentrations [9, 13], and the measurement of the photovoltaic current density has been reported to be linear up to reduction degrees of approximately unity for crystals with a comparable total iron concentration [22]. Our observation therefore complies with existing literature. However, the explanation of the absence of gratings at reduction degrees higher than 3 is not straightforward and, to the best of our knowledge, unreported so far. As mentioned before, the behavior cannot be solely explained by a lack of electron trap centers, because even in sample 9, we have an Fe^{3+} concentration of more than $1 \times 10^{18} cm^{-3}$.

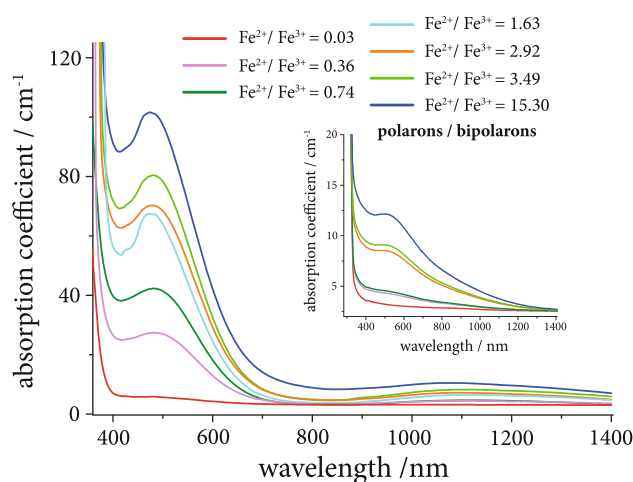


Fig. 5 Absorption spectra for samples with increasing reduction degree; it can be seen that the reduced samples not only possess an increasing absorption in the visible due to the higher Fe^{2+} concentration, but also a strong absorption shoulder due to the occurrence of polarons/bipolarons (*inset*)

The effect was reproducible and has also been verified by using the two-beam coupling setup described in [10], where, again, not even a transient diffracted beam was observed. As a possible explanation, thermal effects may be suspected as being responsible for a premature erasure of the grating. These effects can be ruled out by simulations that show an amplitude of the thermal grating which is lower than 1 mK, so that pyroelectric fields can be neglected. Moreover, even if the simulations predict a maximum average temperature increase of about 35 K, its time constant is too large (about 4 min) to justify the absence of any refractive index grating formation already at the beginning of the recording process. Therefore, the most likely explanation is a significant increase in the conductivity in the more reduced samples due to the increase in both Fe^{2+} and polaron/bipolaron concentration. By fitting each spectrum as the superposition of the absorption bands due Fe^{2+} (centered at 466 and 1,100 nm) and the bipolaron/polaron bands (centered at about 495 and 755 nm, respectively), it was possible to remove the absorption due to iron, thus highlighting the increased bipolaron/polaron contribution, as reported in the inset of Fig. 5. The possible incorporation of hydrogen during the process with the Ar(98 %) + H_2 (2 %) mixture is another subject of further investigations, although in many

previous experiments, the presented reduction treatment has been successfully applied [23, 24].

4.3 Photoconductivity

Figure 6 shows the inverse time constant as a function the reduction degree, which is an indicator of a crystal's photoconductivity. It is clearly visible in the inset of Fig. 6 that for the first four samples (up to a reduction degree of 0.36), the conductivity rises linearly with the reduction degree, while for higher Fe^{2+} content, the conductivity increases in a superlinear fashion, pointing again at additional mechanisms of charge generation, possibly due to an increased polaron/bipolaron contribution. However, the effect is not yet fully understood and is being further investigated. In this context, it is important to mention that even for the samples with a reduction degree exceeding unity, the dark conductivity is negligible compared to the photoconductivity, that is no substantial grating decay could be observed within minutes, which was the timescale that was investigated for the trapping experiments.

4.4 Dielectrophoretic particle trapping

To test the previous assumptions about their usability, particles are trapped dielectrophoretically on the crystal samples. In order to compare all samples directly and to observe the particle alignment with white light, the writing beam is coupled into a Nikon TE2000 inverted microscope. In this inverted setup, the samples are illuminated from below and the suspension is dripped onto the top surface of the crystal. The samples are illuminated with a binary stripe pattern of $\Lambda = 422 \mu\text{m}$, since binary patterns give the steepest electric field gradients, hence the highest trapping

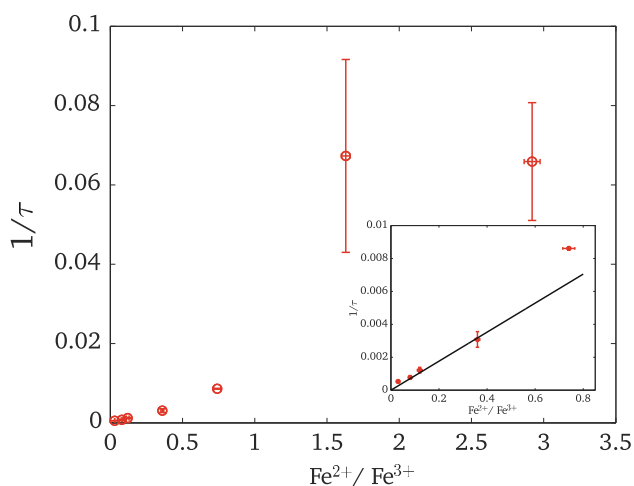


Fig. 6 Conductivity values derived by the inverse of Eq. 1 for different reduction degrees; the inset shows a close-up of the linear regime for the first four samples up to a $\text{Fe}^{2+}/\text{Fe}^{3+}$ ratio of 0.36

powers. Note that in this configuration, it is important to again account for the different thicknesses and absorptions to make sure that the intensity on the top surface is equal for all samples. This is especially important since the DEP force magnitude decays rapidly in the normal direction [25], so only the electric fields on the surface are responsible for trapping.

After being exposed to the light pattern, a suspension of glassy carbon spheres (\varnothing 2–12 μm , Sigma-Aldrich) suspended in insulating tetradecane was dripped onto the samples. Compared to the original illumination pattern, two lines of glassy carbon spheres form within one period (spatial frequency doubling), which is a clear indicator for dielectrophoretic trapping [6, 7]. This behavior can be easily understood by looking at Eq. 2; the force is proportional to the gradient of the squared electric field, so there are two attractive equilibrium positions within each period, as long as the Clausius-Mossotti factor is positive [11]. This is the case when insulating liquid media are used for suspensions in the DC limit. Fig. 7 shows results from the trapping experiments. Note that variations in the overall particle density can result from slightly different droplets sizes dripped onto the crystal. In the measurements, the top surface intensity was kept constant at $233 \pm 5 \text{ mW cm}^{-2}$, but the illumination time was reduced from 30 s for sample

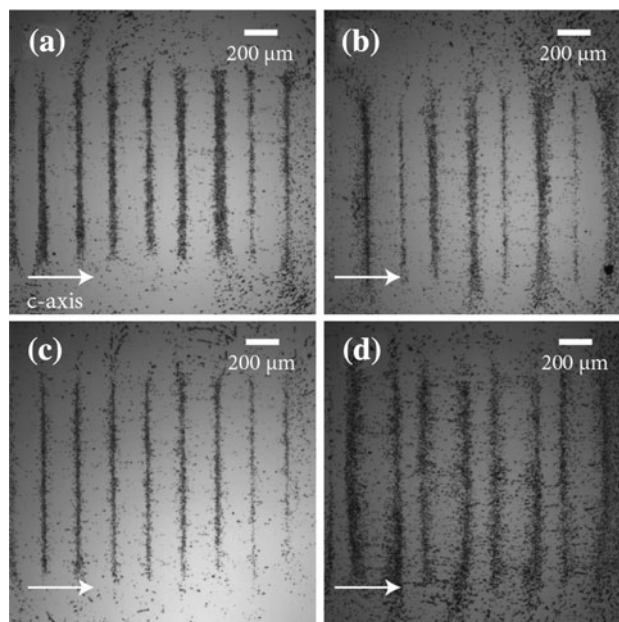


Fig. 7 Particle trapping experiments on reduced crystal samples at illumination power of $233 \pm 5 \text{ mW cm}^{-2}$ **a** as-grown crystal after 30 s **b** sample 151.2 after 9 s **c** sample 151.6.1 after 3 s **d** sample 151.5.1 after 3 s; it is clearly visible that for the first three samples, the writing can be reduced according to the measured photocurrents without a decrease in the trapping efficiency, while the last sample with a reduction degree of 2.92 shows a strong decrease in the particle modulation due to the lower saturation field

ATI with a reduction degree of 0.030 to 9 s for 151.2 (0.12) and 3 s for samples 151.6.1 (0.36) and 151.5.1 (2.92), according to the previously measured values for the photovoltaic current density j_{photo} . It can be seen that the first three samples show very pronounced dielectrophoretic trapping with a comparable trapping efficiency despite the significantly reduced writing times. The sample 151.5.1 also shows DEP trapping, but with a slightly lower trapping contrast, which means that more particles are randomly located in regions where there is no electric field gradient. This observation is in compliance with the previous measurements, from which a lower saturation field, hence lower trapping power, is expected for samples with higher reduction degree than 0.36. This serves as another evidence for the different charge transport mechanisms that must be taken into account with these highly reduced samples.

5 Conclusion

To sum up, crystals with varying reduction degrees up to very high values of $\text{Fe}^{2+}/\text{Fe}^{3+} = 15$ were analyzed using digital holography, which provides direct access to the magnitude and time evolution of the internal space-charge field without any approximation. In the present experiments, several unexpected results were found at reduction degrees higher than 0.36, which deserve further investigation, among them the unexpected change in the magnitude of the saturation field and the saturation of the photovoltaic current density at higher reduction degrees. The effect that is responsible for the prohibition of grating formation in crystals which were reduced to more than 2.92 is yet to be further investigated. Thermal effects due to the laser light absorption could be ruled out by simulations. It is anticipated that additional absorption and charge transport processes due to the occurrence of bipolarons play an important role. As far as the application of $\text{Fe}:\text{LiNbO}_3$ for the use as substrate material in OET is concerned, it could be shown that a moderate reduction degree can significantly speed up the photoconductivity and hence the internal evolution of space-charge fields. Consequently, an intermediate reduction degree between 0.36 and 0.74 at this point appears to be the best trade-off between high internal field magnitude and high photosensitivity. Higher reduction degrees do not yield an increase in the photovoltaic current density, but only a significant decrease in the saturation field, hence the maximum trapping strength. The use of these optimal crystal samples speeds up the response time of the internal fields by more than one order of magnitude without the need for increased laser power which makes such crystals a well-suited substrate material for “in-situ” applications with limited light power.

Acknowledgments The authors would like to thank Marco Bazzan and Maria Vittoria Ciampolillo for fruitful discussions. Financial support from the European Commission in the frame of Photonics4Life, the Deutsche Forschungsgemeinschaft (Grant No. TRR61), the University of Padova (Prog. Ateneo CPDA073231/07) and the Italian Ministry of University and Research (PRIN08, prot. 20088ZA8H9_002) is gratefully acknowledged.

References

1. A. Ashkin, Acceleration and trapping of particles by radiation pressure, *Phys. Rev. Lett.* **24**, 156–159 (1970)
2. A. Ashkin, J.M. Dziedzic, J.E. Bjorkholm, S. Chu, Observation of a single-beam gradient force optical trap for dielectric particles. *Opt. Lett.* **11**, 288–290 (1986)
3. D.G. Grier, A revolution in optical manipulation. *Nature* **424**, 810–816 (2003)
4. P. Chiou, A. Ohta, M. Wu, Massively parallel manipulation of single cells and microparticles using optical images. *Nature* **436**, 370–372 (2005)
5. H. Pohl, Some effects of nonuniform fields on dielectrics. *J. Appl. Phys.* **29**, 1182–1188 (1958)
6. H.A. Eggert, F.Y. Kuhnert, K. Buse, J.R. Adleman, D. Psaltis, Trapping of dielectric particles with light-induced space-charge fields. *Appl. Phys. Lett.* **90**, 241909 (2007)
7. M. Esseling, F. Holtmann, M. Woerdemann, C. Denz, Two-dimensional dielectrophoretic particle trapping in a hybrid crystal/PDMS-system. *Opt. Express* **18**, 17404–17411 (2010)
8. B.I. Sturman, V.M. Fridkin, *The Photovoltaic and Photorefractive Effects in Noncentrosymmetric Materials*. (Gordon & Breach Science Publishers, New York, 1992)
9. K. Peithmann, A. Wiebrock, K. Buse, Photorefractive properties of highly-doped lithium niobate crystals in the visible and near-infrared. *Appl. Phys. B* **68**, 777–784 (1999)
10. A. Zaltron, M. Bazzan, N. Argiolas, M.V. Ciampolillo, C. Sada, Depth-resolved photorefractive characterization of lithium niobate crystals doped with iron by thermal diffusion. *Appl. Phys. B* **108**, 657–663 (2012)
11. S. Glaesener, M. Esseling, C. Denz, Multiplexing and switching of virtual electrodes in optoelectronic tweezers based on LiNbO_3 . *Opt. Lett.* **37**, 3744–3746 (2012)
12. P. Günter, *Photorefractive Materials and Their Applications 2*, (Springer, New York, 2007)
13. E. Krätzig, Photorefractive effect and photoconductivity in $\text{LiNbO}_3:\text{Fe}$. *Ferroelectrics* **21**, 635–636 (1978)
14. N.V. Kukhtarev, V.B. Markov, S.G. Odulov, M.S. Soskin, V.L. Vinetskii, Holographic storage in electrooptic crystals 1: steady state. *Ferroelectrics* **22**, 949–960 (1979)
15. M.V. Ciampolillo, A. Zaltron, M. Bazzan, N. Argiolas, C. Sada, Quantification of iron (Fe) in lithium niobate by optical absorption. *Appl. Spectrosc.* **65**, 216–220 (2011)
16. H. Kurz, E. Krätzig, E.W. Keune, H. Engelmann, U. Gonser, B. Dischler, A. Rüber, Photorefractive centers in LiNbO_3 , studied by optical-, Mössbauer- and EPR-methods. *Appl. Phys.* **12**, 355–366 (1977)
17. B. Kemper, von G. Bally, Digital holographic microscopy for live cell applications and technical inspection. *Appl. Opt.* **47**, A52–A61 (2008)
18. M. de Angelis, S. De Nicola, A. Finizio, G. Pierattini, P. Ferraro, S. Pelli, G. Righini, S. Sebastiani, Digital-holography refractive-index-profile measurement of phase gratings. *Appl. Phys. Lett.* **88**, 111114 (2006)

19. M. Esseling, S. Glasener, F. Volonteri, C. Denz, Opto-electric particle manipulation on a bismuth silicon oxide crystal. *Appl. Phys. Lett.* **100**, 161903 (2012)
20. T. Jones, *Electromechanics of Particles*. (Cambridge University Press, Cambridge, 1995)
21. K. Peithmann, N. Korneev, M. Flaspöhler, K. Buse, and E. Krätzig, Investigation of small polarons in reduced iron-doped lithium niobate crystals by non-steady-state photocurrent technique, *Phys. Status Solidi A* **178**(1), r1–r3 (2000)
22. R. Sommerfeldt, L. Holtmann, E. Krätzig, B.C. Grabmeier, Influence of Mg doping and composition on the light-induced charge transport in LiNbO_3 . *Phys. Status Solidi A* **106**, 89–98 (1988)
23. M.V. Ciampolillo, A. Zaltron, M. Bazzan, N. Argiolas, C. Sada, M. Bianconi, Lithium niobate crystals doped with iron by thermal diffusion: relation between lattice deformation and reduction degree. *J. Appl. Phys.* **107**, 084108 (2010)
24. M.V. Ciampolillo, A. Zaltron, M. Bazzan, N. Argiolas, C. Sada, S. Mignoni, M. Fontana, Iron doping of lithium niobate by thermal diffusion from thin film: study of the treatment effect. *Appl. Phys. Mater. Sci. Process.* **104**, 453–460 (2011)
25. J.K. Valley, A. Jamshidi, A.T. Ohta, H.-Y. Hsu, M.C. Wu, Operational regimes and physics present in optoelectronic tweezers. *J. Microelectromech. Syst.* **17**, 342–350 (2008)